

Research Article

A New Approach for Free Vibration Analysis of Thin-Walled Box Girder Considering Shear Lag Effect

Zuolong Luo ¹, Haoyun Yuan,² and Xirong Niu¹

¹Department of Civil Engineering, Shanxi University, Taiyuan 030000, China

²Department of Bridge Engineering, Chang'an University, Xi'an 710064, China

Correspondence should be addressed to Zuolong Luo; luozuolong@sxu.edu.cn

Received 12 December 2018; Accepted 21 January 2019; Published 12 February 2019

Academic Editor: Evangelos J. Sapountzakis

Copyright © 2019 Zuolong Luo et al. This is an open access article distributed under the Creative Commons Attribution License, which permits unrestricted use, distribution, and reproduction in any medium, provided the original work is properly cited.

The thin-walled box girder (T-WBG) is widely applied in the long-span bridge structures during the past decades due to its lighter self-weight and better mechanical properties. The shear lag effect (SLE), an essential aspect of T-WBG which governs the stress and the deformation, is rather necessary to be revealed properly. The extraordinary issue of T-WBG analysis nowadays is the SLE impact on its dynamical response to external load. This paper proposes an improved finite element method (FEM) to obtain the realistic vibration characteristics of the T-WBG considering the SLE by theory analysis and formula derivation. Firstly, based on the classical plate and shell theory as well as beam theory, the T-WBG was divided into shell subunit for the roof and beam subunit for web and floor, respectively. Secondly, a 3-order polynomial which is consistent with the experiment results was adopted as the axial-displacement interpolation function of the roof subunit, whose nodal displacements parameters were also taken as the basic. Thirdly, the nodal displacement parameters of the web subunit and floor subunit were deduced by the basic according to the principle of deflection consistency. It is shown through a numerical example that the proposed method is much more economical to achieve reasonable accuracy than traditional FEM analysis software when dealing with the free vibration problem of the T-WBG considering the SLE. Besides, it is also observed that the natural frequency values considering the SLE have a trend of decreasing markedly in general, and the influence of SLE on higher-order frequency is more significant than on the lower one under the boundary condition of cantilever supported, while a contrary effect under the boundary condition of simple supported.

1. Introduction

SLE was first noticed in aerospace structural engineering practice, which has a direct impact on the detailed structural design of T-WBG accessory structures such as wing spar and flap [1–3]. In order to reduce self-weight and increase spanning capacity, T-WBG structures nowadays are extensively used in long-span bridges, and the SLE investigation has become extremely important in design and construction of such bridges [4–10]. This is because (1) the T-WBG used in long-span bridges becomes more flexible as the span becomes longer, leading to a remarkable increase in SLE; (2) the width-span ratios of the long-span bridges are generally larger nowadays, and theoretical study and experimental observations suggest that the SLE is prone to occur in T-WBG with a large width-span ratio. At present, the T-WBG is widely used in long-span bridges, and its dynamical response to

pedestrian load, vehicle load, and so on is much more complex than the static one, which indicates that the vibration analysis of the T-WBG considering the SLE has become a hot spot in the research field. During the past decades, much effort has been directed towards SLE analysis of the T-WBG. Among these methods [11–24], the energy variation method (EVM) and the FEM are considered to be two of the most widely used methods.

For the EVM, numerous studies have contributed to its development. Reissner [25] firstly proposed the EVM for SLE. In his study, a second-order polynomial was used as an approximate axial-displacement interpolation function, trying to describe the actual longitudinal displacement mode considering the SLE. An improved sequential Reissner approach validated by model test and numerical analysis was presented by Guo et al. [26], which used a third-order polynomial as the distribution function. Further research

was carried out by Chang [27], in which superposition principle is used to account for the prestress influence on SLE. While these methods above are adopted to deal with SLE problems, difficulties are encountered. These difficulties are (1) the EVM method is not applicable to section-altered box girder due to the inability for a closed solution achieving; (2) the result reliability is difficult to evaluate and a further revision to the result is not easy; and (3) the EVM theory is complicated such that it is not convenient for an engineering application.

As for the FEM, several methods have been established as an attempt to overcome the problems in the EVM. Jing et al. [28] proposed a FEM for SLE analysis in section-altered box girder with long overhanging flange and demonstrated the capacity of the FEM application to the SLE analysis of section-altered box girder. Tenchev [29] compared the performance of the FEM in SLE analysis with that of model test results and confirmed the results reliability of the FEM. Luo [30] originally presented a FEM-based method called finite segment method, in which a semianalytical finite segment model of planar beam element was established, reducing the three-dimension problem to one-dimension problem, leading to an easier FEM application to SLE analysis. Although some progress has been made in the FEM for SLE analysis of T-WBG, there are mainly two issues remaining. First, the axial-displacement interpolation function, which is directly correlated with the accuracy of the results, is not adequately and reasonably chosen in the FEM. Second, the result accuracy of the FEM is highly dependent on the overall numbers of degrees of freedom (DOFs). Generally speaking, to achieve a valid FEM result, the total element DOF numbers must be "huge and plenty," which leads to a long computation time in modeling and solving. Third, in order to obtain a relatively accurate solution, an enough dense meshing is customarily conducted, resulting in a great increase of DOFs, which may bring out singularity of the result, sometimes even with wrong conclusions.

To the best of the authors' knowledge, much more studies aiming at solving the static response of the T-WBG considering the SLE have been conducted, while there have been relatively few research studies for the SLE impact on dynamic characteristic of the T-WBG. So, this paper presents an improved FEM for free vibration analysis of T-WBG considering the SLE, in which the roof subunit was modeled as plate element, and the web subunit and floor subunit were simulated as beam elements, respectively. The nodal displacement parameters of the subunits were all only determined by the basic parameters of the roof subunit, resulting in a dramatically decrease in overall element DOFs. A 3-order polynomial was used as an interpolation function for axial-displacement interpolation function, which conforms to the actual axial-displacement mode caused by SLE. The element integral stiffness matrix was deduced on the basis of variation principle. To show the accuracy of the proposed method, the first six natural frequency parameters of the same T-WBG as [31] were calculated for comparison. Besides, an engineering example was studied for the accuracy and efficiency verification of the proposed method, and some valuable conclusions for SLE effect on

natural frequency considering the boundary conditions are also achieved.

2. The Proposed Method

The proposed method is a hybrid approach, consisting of the methods for solving planar stress problem and thin plate bending problem with small deflection. This method is based on three key concepts: (1) the roof subunit is modeled as the plate element whose stress state can be superposed by planar stress state and thin plate bending state with small deflection; (2) the roof subunit is seen as the basic element, whose nodal translation and rotation DOFs are taken as the basic parameters; (3) the web subunit and floor subunit are simulated as beam elements whose displacement parameters can be derived from that of the roof subunit according to the principle of deflections consistency. Figure 1 shows the principle of the proposed method.

2.1. The Nodal Displacement Mode of Roof Subunit. The nodal translation and rotation DOFs of the roof subunit can be written as follows:

$$\delta = [\delta_1 \quad \delta_2 \quad \delta_3 \quad \delta_4]^T, \quad (1)$$

where $\delta_i = [u_i \quad v_i \quad \omega_i \quad \theta_{xi} \quad \theta_{yi}]$, ($i = 1, 2, 3, 4$) and u_i , v_i , ω_i , θ_{xi} , θ_{yi} are the nodal axial displacement, transverse displacement, vertical displacement, rotational displacement around x -axis, and rotational displacement around y -axis, respectively, as shown in Figure 2.

In order to analyze the SLE more accurately, a 3-order polynomial conforms to the actual displacement mode was taken as the axial-displacement interpolation function of the roof subunit. For the cross section shown in Figure 3, the axial displacement at any node of the roof subunit can be expressed as follows:

$$u(y) = \frac{1}{2}(u_4 - u_1)\xi^3 + \frac{1}{2}(u_4 + u_1), \quad (2)$$

where $\xi = (2y/k)$ is the node transverse coordinate in local coordinate system and k is the transverse width of the basic element.

The Lagrange interpolation function is used as the interpolation function of vertical displacement and rotational displacement; the shape function of the element can be expressed by the local coordinate system as follows:

$$\mathbf{N} = [N_{i,j}]_{5 \times 20}. \quad (3)$$

Due to space limitations, the elements in the matrix \mathbf{N} are not listed here.

The stiffness matrix of the roof subunit in planar stress state can be obtained as follows:

$$\mathbf{K}_p^e = tdk \int_{-1}^1 \int_{-1}^1 \mathbf{B}_p^T \mathbf{D}_p \mathbf{B}_p d\xi d\eta, \quad (4)$$

where t , d , and k are the thickness, element length in x -axis direction, and element width in y -axis direction, respectively, and \mathbf{B}_p and \mathbf{D}_p are the strain matrix and elastic matrix of the roof in planar stress state.

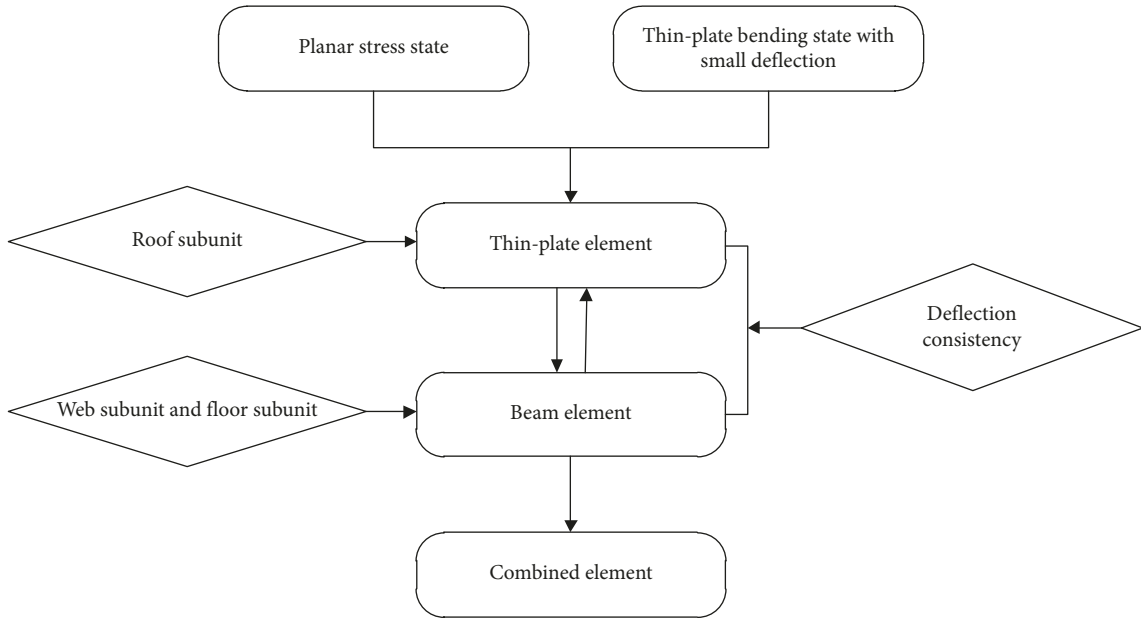


FIGURE 1: Principle of the proposed method.

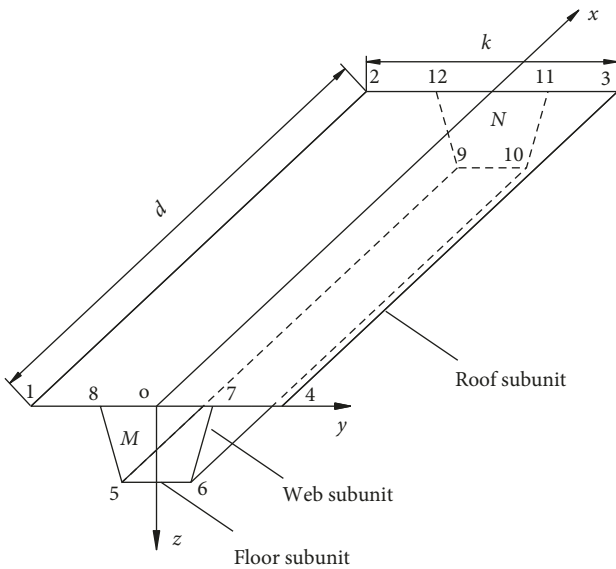


FIGURE 2: Layout of the basic element.

The stiffness matrix of the roof subunit in thin plate bending state with small deflection can be obtained as follows:

$$\mathbf{K}_B^e = \int_{-(t/2)}^{t/2} \int_{-1}^1 \int_{-1}^1 \mathbf{B}_B^T \mathbf{D}_P \mathbf{B}_B d\xi d\eta dz, \quad (5)$$

where \mathbf{B}_B is the strain matrix of the roof in thin plate bending state with small deflection.

2.2. The Nodal Displacement Mode of Web Subunit. All the plates that constitute the web subunit bear the loads together, and the stress of a single plate is reflected by the beam stress characteristic, which suggests that each plate making

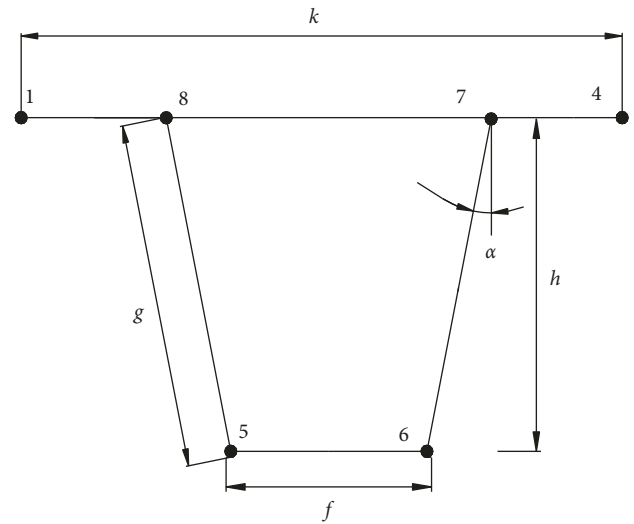


FIGURE 3: Cross section layout of the basic element.

up the web subunit can be simulated by beam element. In addition, the web subunit plays a primary part in vertical stiffening on the roof subunit for its high aspect ratio such that only vertical displacement and axial displacement are taken into consideration.

As is shown in Figure 2, each plate making up the web subunit uses a polynomial of the degree one and a cubic polynomial as axial displacement mode and vertical displacement mode, respectively, and the interpolating functions are as follows:

$$\begin{aligned} \mathbf{m} &= [1 - \zeta \ \zeta], \\ \mathbf{n} &= [1 - 3\zeta^2 + 2\zeta^3 \ (\zeta - 2\zeta^2 + \zeta^2)d \ 3\zeta^2 - 2\zeta^3 \ (3\zeta^3 - \zeta^2)d], \end{aligned} \quad (6)$$

where $\zeta = x/d$.

Each nodal displacement parameter can be obtained according to the principle of deflections consistency between the roof subunit and web subunit, and the axial displacement parameters of nodes 7 and 8 are obtained on the basis of equations (1)–(3), which are as follows:

$$u_7 = \frac{1}{2L^3} (u_4 - u_1) (k - s)^3 + \frac{1}{2} (u_4 + u_1), \quad (7)$$

$$u_8 = \frac{1}{2L^3} (u_4 - u_1) (s - k)^3 + \frac{1}{2} (u_4 + u_1). \quad (8)$$

Similarly, the angular displacements around y -axis of nodes 7 and 8 are as follows:

$$\theta_{y7} = \frac{1}{2} \left(1 - \frac{a}{k}\right) \theta_{y1} + \frac{1}{2} \left(1 + \frac{a}{k}\right) \theta_{y4}, \quad (9)$$

$$\theta_{y8} = \frac{1}{2} \left(1 + \frac{a}{k}\right) \theta_{y1} + \frac{1}{2} \left(1 - \frac{a}{k}\right) \theta_{y4}. \quad (10)$$

The vertical displacements of nodes 7 and 8 can also be organized by equations (1)–(3), which can be expressed as follows:

$$\begin{aligned} u_7 = & \frac{1}{4} \left(1 - \frac{a}{k}\right) \left[2 - \frac{a}{c} - \left(\frac{a}{k}\right)^2\right] \omega_1 + \frac{k}{8} \left(1 - \frac{a}{k}\right) \left[1 - \left(\frac{a}{k}\right)^2\right] \theta_{x1} \\ & + \frac{1}{4} \left(1 + \frac{a}{k}\right) \left[2 + \frac{a}{k} - \left(\frac{a}{k}\right)^2\right] \omega_4 - \frac{k}{8} \left(1 + \frac{a}{k}\right) \left[1 - \left(\frac{a}{k}\right)^2\right] \theta_{x4}, \end{aligned} \quad (11)$$

$$\begin{aligned} u_8 = & \frac{1}{4} \left(1 + \frac{a}{k}\right) \left[2 + \frac{a}{k} - \left(\frac{a}{k}\right)^2\right] \omega_1 + \frac{k}{8} \left(1 + \frac{a}{k}\right) \left[1 - \left(\frac{a}{k}\right)^2\right] \theta_{x1} \\ & + \frac{1}{4} \left(1 - \frac{a}{k}\right) \left[2 - \frac{a}{k} - \left(\frac{a}{k}\right)^2\right] \omega_4 - \frac{k}{8} \left(1 - \frac{a}{k}\right) \left[1 - \left(\frac{a}{k}\right)^2\right] \theta_{x4}. \end{aligned} \quad (12)$$

The left web and right web of the web subunit are all regarded as beam elements, and the angular displacements around y -axis at M end (as shown in Figure 2) are identical with that of nodes 7 and 8. The centroid angular displacement of the floor subunit around y -axis is linearly interpolated between nodes 5 and 6, which is in line with the two basic assumption of beam element: (1) the longitudinal fiber squeeze of the beam element is not taken into consideration; (2) the rotation angle of each beam section is the same. The angular displacements of the left web and right web around y -axis at M end are given as follows:

$$\theta_{lcm} = \frac{1}{2} \left(1 + \frac{a}{k}\right) \theta_{y1} + \frac{1}{2} \left(1 - \frac{a}{k}\right) \theta_{y4}, \quad (13)$$

$$\theta_{rcm} = \frac{1}{2} \left(1 - \frac{a}{k}\right) \theta_{y1} + \frac{1}{2} \left(1 + \frac{a}{k}\right) \theta_{y4}, \quad (14)$$

$$\theta_{bcm} = \frac{1}{2} \theta_{lcm} + \frac{1}{2} \theta_{rcm}. \quad (15)$$

The axial displacements of the left web and right web at M end are expressed as follows:

$$u_{lcm} = u_8 - \frac{h}{2} \theta_{lcm}, \quad (16)$$

$$u_{rcm} = u_7 - \frac{h}{2} \theta_{rcm}. \quad (17)$$

The axial displacements of nodes 5 and 6 are as follows:

$$u_5 = u_8 - h \theta_{lcm}, \quad (18)$$

$$u_6 = u_7 - h \theta_{rcm}. \quad (19)$$

The centroid axial displacement of the floor subunit at M end is linearly interpolated between nodes 5 and 6, which is as follows:

$$u_{bcm} = \frac{1}{2} u_5 + \frac{1}{2} u_6. \quad (20)$$

The vertical displacements of the left web and right web at M end are the same as that of nodes 7 and 8, which can be represented as follows:

$$\omega_{lcm} = \omega_8, \quad (21)$$

$$\omega_{rcm} = \omega_7. \quad (22)$$

The centroid vertical displacement of the floor subunit at M end is linearly interpolated between nodes 5 and 6, which is as follows:

$$\omega_{bcm} = \frac{1}{2} \omega_{lcm} + \frac{1}{2} \omega_{rcm}. \quad (23)$$

By using the same method, the displacement mode of each plate at N end (as shown in Figure 2) can also be obtained.

With regard to the left web, let \mathbf{u}_1^* , ω_1^* be the axial displacement parameter and vertical displacement parameter of the centroid, respectively, which are as follows:

$$\mathbf{u}_1^* = [u_{lcm} \quad u_{lcn}]^T, \quad (24)$$

$$\omega_1^* = [\omega_{lcm} \quad \theta_{lcm} \quad \omega_{lcn} \quad \theta_{lcn}]^T. \quad (25)$$

The axial displacement and vertical displacement of the left web are as follows:

$$u_{lc} = \mathbf{nu}_1^* = \mathbf{A}\boldsymbol{\delta}, \quad (26)$$

$$\omega_{lc} = \mathbf{m}\omega_1^* = \mathbf{B}\boldsymbol{\delta},$$

where \mathbf{A} is the transformation matrix of \mathbf{u}_1^* and $\boldsymbol{\delta}$, which can be obtained on the basis of equations (1), (8), (13), (16), and (24) and \mathbf{B} is the transformation matrix of ω_1^* and $\boldsymbol{\delta}$, which can also be obtained based on equations (1), (10), (13), (21), and (25). The elements of matrix \mathbf{A} and \mathbf{B} are as follows:

$$A_{1,1} = \frac{a(1-\zeta)}{2d^3},$$

$$A_{1,5} = -\frac{h(k+a)}{4d},$$

$$A_{1,6} = \frac{a\zeta}{2d^3},$$

$$A_{1,10} = -\frac{h(k+a)}{4d},$$

$$A_{1,11} = \frac{a\zeta}{2d^3},$$

$$A_{1,15} = -\frac{h(k+a)}{4d},$$

$$A_{1,16} = \frac{a(1-\zeta)}{2d^3},$$

$$A_{1,20} = -\frac{h(k+a)}{4d},$$

$$B_{1,3} = \frac{1}{4}(1-3\zeta^2+2\zeta^3)\left(1+\frac{a}{k}\right)\left[2+\frac{a}{k}-\left(\frac{a}{k}\right)^2\right],$$

$$B_{1,4} = \frac{k}{8}(1-3\zeta^2+2\zeta^3)\left(1+\frac{a}{k}\right)\left[1-\left(\frac{a}{k}\right)^2\right],$$

$$B_{1,5} = \frac{d}{2}(\zeta-2\zeta^2+\zeta^3)\left(1+\frac{a}{k}\right),$$

$$B_{1,8} = \frac{1}{4}(3\zeta^2-2\zeta^3)\left(1+\frac{a}{k}\right)\left[2+\frac{a}{k}-\left(\frac{a}{k}\right)^2\right],$$

$$B_{1,9} = \frac{1}{8}(3\zeta^2-2\zeta^3)\left(1+\frac{a}{k}\right)\left[1-\left(\frac{a}{k}\right)^2\right],$$

$$B_{1,10} = \frac{d}{2}(-\zeta^2+\zeta^3)\left(1+\frac{a}{k}\right),$$

$$B_{1,13} = \frac{1}{4}(3\zeta^2-2\zeta^3)\left(1-\frac{a}{k}\right)\left[2-\frac{a}{k}-\left(\frac{a}{k}\right)^2\right],$$

$$B_{1,14} = \frac{1}{8}(3\zeta^2-2\zeta^3)\left(1-\frac{a}{k}\right)\left[1-\left(\frac{a}{k}\right)^2\right],$$

$$B_{1,15} = \frac{d}{2}(-\zeta^2+\zeta^3)\left(1-\frac{a}{k}\right),$$

$$B_{1,18} = \frac{1}{4}(1-3\zeta^2+2\zeta^3)\left(1-\frac{a}{k}\right)\left[2-\frac{a}{k}-\left(\frac{a}{k}\right)^2\right],$$

$$B_{1,19} = \frac{k}{8}(1-3\zeta^2+2\zeta^3)\left(1-\frac{a}{k}\right)\left[1-\left(\frac{a}{k}\right)^2\right],$$

$$B_{1,20} = \frac{d}{2}(\zeta-2\zeta^2+\zeta^3)\left(1-\frac{a}{k}\right),$$

$$B_{2,3} = \frac{1}{4d}(-6\zeta+6\zeta^2)\left(1+\frac{a}{k}\right)\left[2+\frac{a}{k}-\left(\frac{a}{k}\right)^2\right],$$

$$B_{2,4} = \frac{k}{8d}(-6\zeta+6\zeta^2)\left(1+\frac{a}{k}\right)\left[1-\left(\frac{a}{k}\right)^2\right],$$

$$B_{2,5} = \frac{d}{2}(1-4\zeta+3\zeta^2)\left(1+\frac{a}{k}\right),$$

$$B_{2,8} = \frac{1}{4l}(6\zeta-6\zeta^2)\left(1+\frac{a}{k}\right)\left[2+\frac{a}{k}-\left(\frac{a}{k}\right)^2\right],$$

$$B_{2,9} = \frac{1}{8l}(6\zeta-6\zeta^2)\left(1+\frac{a}{k}\right)\left[1-\left(\frac{a}{k}\right)^2\right],$$

$$B_{2,10} = \frac{d}{2}(3\zeta^2-2\zeta)\left(1+\frac{a}{k}\right),$$

$$B_{2,13} = \frac{1}{4l}(6\zeta-6\zeta^2)\left(1-\frac{a}{k}\right)\left[2-\frac{a}{k}-\left(\frac{a}{k}\right)^2\right],$$

$$B_{2,14} = \frac{1}{8l}(6\zeta-6\zeta^2)\left(1-\frac{a}{k}\right)\left[1-\left(\frac{a}{k}\right)^2\right],$$

$$B_{2,15} = \frac{d}{2}(3\zeta^2-2\zeta)\left(1-\frac{a}{k}\right),$$

$$B_{2,18} = \frac{1}{4l}(6\zeta^2-6\zeta)\left(1-\frac{a}{k}\right)\left[2-\frac{a}{k}-\left(\frac{a}{k}\right)^2\right],$$

$$B_{2,19} = \frac{k}{8l}(6\zeta^2-6\zeta)\left(1-\frac{a}{k}\right)\left[1-\left(\frac{a}{k}\right)^2\right],$$

$$B_{2,20} = \frac{d}{2}(1-4\zeta+3\zeta^2)\left(1-\frac{a}{k}\right).$$

(27)

The remaining elements are zero without exception.

As for the right web, let \mathbf{u}_r^* , $\mathbf{\omega}_r^*$ be the axial displacement parameter and vertical displacement parameter of the centroid, respectively, which are as follows:

$$\mathbf{u}_r^* = [u_{rcm} \ u_{rcn}]^T, \quad (28)$$

$$\mathbf{\omega}_r^* = [\omega_{rcm} \ \theta_{rcm} \ \omega_{rcn} \ \theta_{rcn}]^T. \quad (29)$$

The axial displacement and vertical displacement of the right web are as follows:

$$u_{rc} = \mathbf{nu}_r^* = \mathbf{nC}\boldsymbol{\delta}, \quad (30)$$

$$\omega_{rc} = \mathbf{m}\boldsymbol{\omega}_r^* = \mathbf{mD}\boldsymbol{\delta},$$

where \mathbf{C} is the transformation matrix of \mathbf{u}_r^* and $\boldsymbol{\delta}$, which can be obtained on the basis of equations (1), (7), (14), (17), and (28) and \mathbf{D} is the transformation matrix of $\mathbf{\omega}_r^*$ and $\boldsymbol{\delta}$, which can also be obtained based on equations (1), (9), (14), (22),

and (29). Due to space limitations, the elements of matrix \mathbf{C} and \mathbf{D} are not listed here.

2.3. The Nodal Displacement Mode of Floor Subunit. To the floor, let \mathbf{u}_b^* , $\boldsymbol{\omega}_b^*$ be the axial displacement parameter and vertical displacement parameter of the centroid, respectively, which are as follows:

$$\mathbf{u}_b^* = [u_{bcn} \quad u_{bcn}]^T, \quad (31)$$

$$\boldsymbol{\omega}_b^* = [\omega_{bcn} \quad \theta_{bcn} \quad \omega_{bcn} \quad \theta_{bcn}]^T. \quad (32)$$

The axial displacement and vertical displacement of the centroid are as follows:

$$\begin{aligned} u_{bc} &= \mathbf{n}\mathbf{u}_b^* = \mathbf{nE}\boldsymbol{\delta}, \\ \omega_{bc} &= \mathbf{m}\boldsymbol{\omega}_b^* = \mathbf{mF}\boldsymbol{\delta}, \end{aligned} \quad (33)$$

where \mathbf{E} is the transformation matrix of \mathbf{u}_b^* and $\boldsymbol{\delta}$, which can be obtained on the basis of equations (1), (7), (8), (13), (14), (18)–(20), and (31) and \mathbf{F} is the transformation matrix of $\boldsymbol{\omega}_b^*$ and $\boldsymbol{\delta}$, which also can be obtained based on equations (1), (11)–(15), (21)–(23), and (32). Also due to space limitations, the elements of matrix \mathbf{E} and \mathbf{F} are not listed here.

Based on the displacement modes of the web subunit and floor subunit, the stiffness contributions to element stiffness matrix of the two can be obtained by the minimum potential energy principle, the expression of which is as follows:

$$\Pi = \Pi_r + \Pi_w + \Pi_f - \mathbf{F}^{eT}\boldsymbol{\delta}, \quad (34)$$

where Π_r is the strain energy of the roof subunit and Π_w and Π_f are the strain energy of the web subunit and floor subunit, respectively, which can be written as follows:

$$\begin{aligned} \Pi_w &= \frac{1}{2} \int_0^d EA_l (\mathbf{n}'\mathbf{u}_l^*)^2 dx + \frac{1}{2} \int_0^d EI_{yl} (\mathbf{m}'\boldsymbol{\omega}_l^*)^2 dx \\ &\quad + \frac{1}{2} \int_0^d EA_r (\mathbf{n}'\mathbf{u}_r^*)^2 dx + \frac{1}{2} \int_0^d EI_{yr} (\mathbf{m}'\boldsymbol{\omega}_r^*)^2 dx, \\ &= \frac{1}{2} \boldsymbol{\delta}^T \mathbf{K}_w^e \boldsymbol{\delta}, \end{aligned} \quad (35)$$

$$\begin{aligned} \Pi_f &= \frac{1}{2} \int_0^d EA_f (\mathbf{n}'\mathbf{u}_f^*)^2 dx + \frac{1}{2} \int_0^d EI_{yf} (\mathbf{m}'\boldsymbol{\omega}_f^*)^2 dx \\ &= \frac{1}{2} \boldsymbol{\delta}^T \mathbf{K}_f^e \boldsymbol{\delta}, \end{aligned} \quad (36)$$

where EA_l , EA_r , and EA_b are the compressive stiffness of the left web, right web, and floor, respectively; EI_{yl} , EI_{yr} , and EI_{yb} are the bending stiffness of the left web, right web, and floor, respectively; \mathbf{K}_w^e and \mathbf{K}_f^e are the stiffness matrix of web subunit and floor subunit, respectively; and \mathbf{F}^{eT} is the external load array.

By taking variation on equation (36) and equating it to zero, the stiffness matrix of the web subunit and floor subunit can be obtained as the following:

$$\begin{aligned} \mathbf{K}_w^e &= EA_l \int_0^d \mathbf{A}^T \mathbf{n}'^T \mathbf{n}' \mathbf{A} dx + EI_{yl} \int_0^d \mathbf{B}^T \mathbf{m}'^T \mathbf{m}' \mathbf{B} dx \\ &\quad + EA_r \int_0^d \mathbf{C}^T \mathbf{n}'^T \mathbf{n}' \mathbf{C} dx + EI_{yr} \int_0^d \mathbf{D}^T \mathbf{m}'^T \mathbf{m}' \mathbf{D} dx, \\ \mathbf{K}_f^e &= EA_f \int_0^d \mathbf{E}^T \mathbf{n}'^T \mathbf{n}' \mathbf{E} dx + EI_{yf} \int_0^d \mathbf{F}^T \mathbf{m}'^T \mathbf{m}' \mathbf{F} dx. \end{aligned} \quad (37)$$

The stiffness matrix of the roof subunit can be obtained by superposition of \mathbf{K}_p^e and \mathbf{K}_b^e , which is as follows:

$$\begin{aligned} \mathbf{K}_r^e &= tdk \int_{-1}^1 \int_{-1}^1 \mathbf{B}_p^T \mathbf{D}_p \mathbf{B}_p d\xi d\eta \\ &\quad + \int_{-(t/2)}^{t/2} \int_{-1}^1 \int_{-1}^1 \mathbf{B}_b^T \mathbf{D}_b \mathbf{B}_b d\xi d\eta dz. \end{aligned} \quad (38)$$

2.4. The Dynamic Equilibrium Equation of FEM. The vibration system is subjected to three kinds of forces caused by mass, damping, stiffness, and external loads. The dynamic equilibrium equation of FEM can be obtained by dispersing the dynamic system, which is as follows:

$$\mathbf{M}^e \ddot{\boldsymbol{\delta}} + \mathbf{C}^e \dot{\boldsymbol{\delta}} + \mathbf{K}^e \boldsymbol{\delta} = \mathbf{P}^e, \quad (39)$$

where \mathbf{M}^e , \mathbf{C}^e , and \mathbf{K}^e are the mass matrix, damping matrix, and the element global stiffness matrix, respectively and $\ddot{\boldsymbol{\delta}}$, $\dot{\boldsymbol{\delta}}$, $\boldsymbol{\delta}$, and \mathbf{P}^e are the acceleration vector, velocity vector, displacement vector, and dynamic load vector, respectively.

2.5. The Coefficient Matrix. In actual, the damping has little effect on natural frequency and vibration mode, which indicates that the force induced by damping can be ignored. Therefore, only the mass matrix and stiffness matrix are discussed in the following.

2.5.1. The Element Mass Matrix. The uniform mass matrix is used to analyze the structural vibration, and the method for mass matrix derivation is the same as that of stiffness matrix. Let the material mass density of the element be ρ ; the uniform mass matrix of the roof subunit can be obtained according to the shape function from the planar stress state and thin plate bending state with small deflection, which is as follows:

$$\mathbf{M}_r^e = \mathbf{M}_p^e + \mathbf{M}_b^e = \rho t \iint_{A_u} \mathbf{N}^T \mathbf{N} dx dy + \rho t \iint_{A_u} \mathbf{M}^T \mathbf{M} dx dy, \quad (40)$$

where A_u is the area of roof subunit.

The uniform mass matrix of the web subunit can be obtained in the same way, that is,

$$\begin{aligned} \mathbf{M}_w^e &= \mathbf{M}_l^e + \mathbf{M}_r^e, \\ \mathbf{M}_l^e &= \rho A_l \int_0^d \mathbf{A}^T \mathbf{n}'^T \mathbf{n}' \mathbf{A} dx + \rho A_l \int_0^d \mathbf{B}^T \mathbf{m}'^T \mathbf{m}' \mathbf{B} dx, \\ \mathbf{M}_r^e &= \rho A_r \int_0^d \mathbf{C}^T \mathbf{n}'^T \mathbf{n}' \mathbf{C} dx + \rho A_r \int_0^d \mathbf{D}^T \mathbf{m}'^T \mathbf{m}' \mathbf{D} dx. \end{aligned} \quad (41)$$

The uniform mass matrix of the floor subunit can be obtained in the same way, that is,

$$\mathbf{M}_f^e = \rho A_f \int_0^d \mathbf{E}^T \mathbf{n}'^T \mathbf{n}' \mathbf{E} dx + \rho A_f \int_0^d \mathbf{F}^T \mathbf{m}'^T \mathbf{m}' \mathbf{F} dx, \quad (42)$$

where A_l , A_r , and A_f are the area of left web, right web, and floor area, respectively.

The mass matrix of the whole element can be obtained by addition of \mathbf{M}_r^e , \mathbf{M}_w^e , and \mathbf{M}_f^e . Due to space limitations, the matrix elements are not listed here.

2.5.2. The Element Stiffness Matrix. The stiffness matrix of the whole element can also be obtained by addition of \mathbf{K}_r^e , \mathbf{K}_w^e , and \mathbf{K}_f^e , which have been deduced above. Due to space limitations, the matrix elements are not listed here.

2.6. The Equivalent Nodal Load. If the external load $P_i(\tau)$ ($i = 1, 2, 3, 4$) is directly applied to the 4 nodes of the roof subunit, the load vector can be directly substituted into the finite element equation for calculation. In actual, the external load acting on bridge deck often consist of distributed load $P(x, y, \tau)$ and concentrated load $P(x_i, y_i, \tau)$; the uniform nodal load array produced by the two kinds of load is as follows:

$$\mathbf{P}^e = t \iint_{A_u} \mathbf{M}^T P(x, y, \tau) dx dy + [M(x, y)]^T P(x_i, y_i, \tau). \quad (43)$$

3. Numerical Examples and Discussion

In order to demonstrate the accuracy of the proposed method, the first four dimensionless natural frequencies of the same T-WBG as discussed by Mashat [31] were calculated for comparison. The boundary condition of the following analysis is simply supported, and the geometric properties of the roof subunit, web subunit, and floor subunit, as well as material properties, were taken as the same as the reference. The schematic diagram of the square box beam is shown in Figure 4, and the geometry of square box beam is listed in Table 1. The present results are shown in Table 2 together with the reference results.

According to the comparison between the present results and reference results in Table 2, it is shown that the results obtained using the proposed method are close to the reference, which verifies the accuracy of the proposed method. Besides, the frequency results calculated by the proposed method is generally a little greater than the reference ones, which is because in the proposed method, the web subunit and floor subunit are all subjected to tension force, and the rigidity of the two subunits accordingly increases, leading to an increasing of the system stiffness. Therefore, the present approach is more accurate.

In addition, a typical engineering example was considered in this section for efficiency and accuracy of the proposed method. The example is a concrete T-WBG bridge with a main span of 30 m. The cross section layout of the T-WBG is single-box-single-cell with a long cantilever

which is 3.55 m long and 0.25 m thick. The width and thickness of the floor is 7.1 m and 0.25 m, respectively, and the height and thickness of the web is 2 m and 0.4 m. In order to study the effect of different boundary conditions on SLE, two boundary conditions (cantilever supported and simply supported) are adopted in the following research. The restraint stiffness of the two boundary conditions is fixed by specification parameters of the actual supports. The plan and cross section layouts of the engineering example are shown in Figure 5, and the structural dimensions and material parameters of the engineering example are shown in Table 3.

The SLE analysis of the engineering example was conducted by using the finite element program compiled with the method proposed above (the compiling process of the calculation program is shown in Figure 6). In the program, the bridge was divided into 30 elements in x -direction, and only natural frequencies of undamped free vibration were calculated in order to facilitate the analysis. The natural frequencies of the preceding 6 modes of the engineering example were compared with that calculated by shell model (shell 181) with ANSYS to verify the efficiency and accuracy of the proposed method. The analysis results are given as Tables 4 and 5.

According to the result comparison between the proposed method and shell model established by ANSYS software in Tables 4 and 5, it is shown that the results obtained using the proposed method are close to that using shell model, which verifies the reliability of the proposed method. Besides, the DOF numbers of the proposed method are reduced by 1922 compared with the ANSYS model, which shows the efficiency of the proposed method. In addition, it is concluded from Tables 4 and 5 that the natural frequency values considering the SLE have a trend of decreasing markedly in general, and the extent of the SLE influence on natural frequency varies with different boundary conditions. For the boundary condition of cantilever supported, the SLE effect on higher-order frequency is more significant than on the lower one, while for the simple supported one, the SLE effect on higher-order frequency is less marked than on the lower one.

4. Conclusions

Aiming at the structural free vibration characteristics of the T-WBG considering the SLE, an improved FEM has been developed to perform this study. In the proposed method, the roof subunit, which was seen as the basic part of the structure, was analyzed using the methods for solving planar stress problem and thin plate bending problem with small deflection, and the web subunit and floor subunit were all regarded as the attachment structures, the analytical approach of which was the beam element method. The displacement mode for each subunit was derived, and the element global stiffness matrix was deduced on the basis of energy variation principle. The uniform mass matrix and load matrix of the whole element were further derived, and finally the finite element dynamic equilibrium equations were obtained.

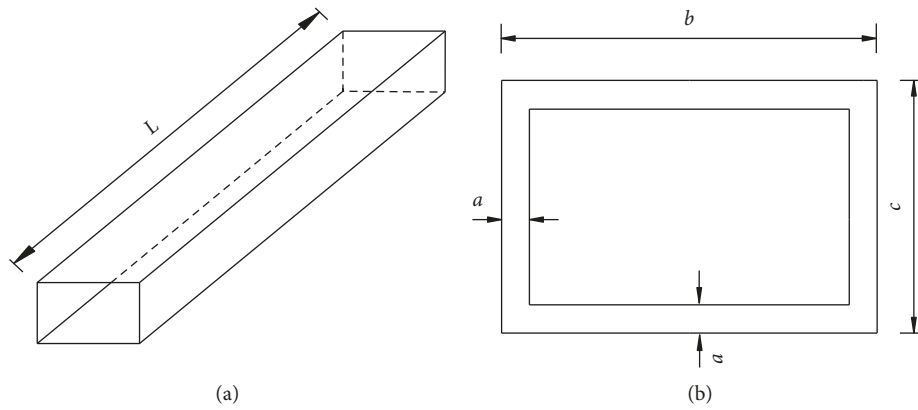


FIGURE 4: Schematic diagram of square box beam: (a) 3-dimensional graph of square box beam; (b) cross section layout of square box beam.

TABLE 1: Geometry of square box beam.

Structural dimensions	L (mm)	a (mm)	b (mm)	c (mm)
Value	76.2/7.62/3.81	0.762	100	100

TABLE 2: Comparison of first four natural frequency parameters in different length-to-thickness ratios for square box beam.

Frequency order	$L/a = 100$		$L/a = 10$		$L/a = 5$	
	R	P	R	P	R	P
1	0.0386	0.0396	0.3803	0.3894	14.5640	14.5692
2	0.0392	0.0401	0.3857	0.3979	14.7350	14.7381
3	2.7011	2.7034	27.0230	27.0285	54.1170	54.1186
4	4.3276	4.3292	43.1800	43.1837	85.9260	85.9273

Note. L/a : the length-to-thickness ratio of the beam; R : reference results; P : present results.

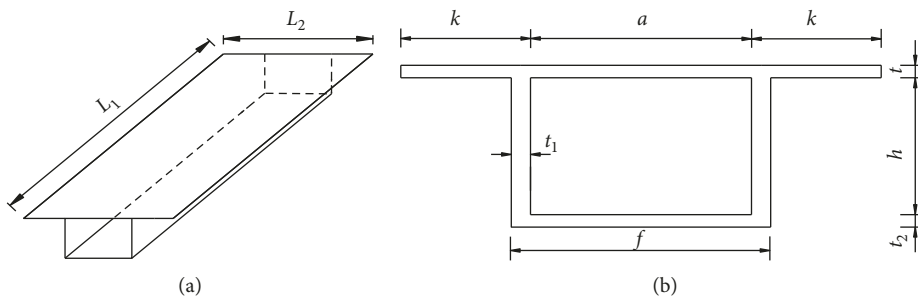


FIGURE 5: Schematic diagram of the engineering example: (a) 3-dimensional graph of T-WBG; (b) cross section layout of T-WBG.

TABLE 3: Structural dimensions and material parameters of the engineering example.

Structural dimensions	L_1 (m)	L_2 (m)	t (mm)	t_1 (mm)	t_2 (mm)	a (mm)	f (mm)	k (mm)	h (mm)	E (MPa)	G (MPa)	ρ (kg/m ³)
Value	30	14.2	250	400	250	7100	7500	3550	2000	35000	15000	2500

A numerical example involving a detailed engineering computational model was presented to demonstrate the efficiency and accuracy of the proposed method. The relevant SLE analysis calculation program was compiled for the

computational model above, as well as a finite element model established with ANSYS software for comparison and verification of the proposed method. The results show that the proposed method exhibited a better performance in

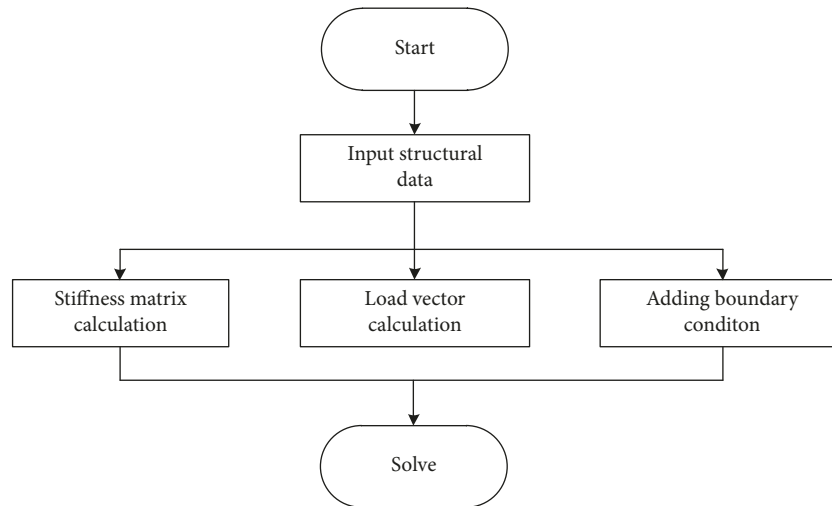


FIGURE 6: Compiling process for the calculation program of the proposed method.

TABLE 4: Natural frequencies comparison for different calculation conditions (cantilever supported).

Frequency order	1	2	3	4	5	6	DOFs
A	5.092	26.074	62.307	102.459	134.845	171.185	2232
B	4.987	26.920	63.178	103.378	145.201	187.422	310
C	13.114	44.609	84.565	127.933	172.556	217.584	—
D	-8.127	-17.689	-21.387	-24.555	-27.355	-30.162	—
E	-61.97%	-39.65%	-25.29%	-19.19%	-15.85%	-13.86%	—

Note. A: ANSYS results; B: present results; C: results of not considering the SLE; D: SLE effect on natural frequencies (B-C); E: proportion of SLE effect on natural frequencies (D/C).

TABLE 5: Natural frequencies comparison for different calculation conditions (simple supported).

Frequency order	1	2	3	4	5	6	DOFs
A	13.397	46.745	87.077	123.913	167.073	194.358	2232
B	13.607	46.598	86.500	128.141	170.199	212.177	310
C	13.824	48.808	93.089	139.796	186.585	232.879	—
D	-0.217	-2.210	-6.589	-11.655	-16.386	-20.702	—
E	-1.57%	-4.53%	-7.08%	-8.34%	-8.78%	-8.89%	—

Note. A: ANSYS results; B: present results; C: results of not considering the SLE; D: SLE effect on natural frequencies (B-C); E: proportion of SLE effect on natural frequencies (D/C).

terms of accuracy and efficiency, as measured by the closeness of the exact values calculated in [31] and by total number of element DOFs compared to the model established with ANSYS. As a result, the proposed method dramatically reduces the number of the DOFs, showing a good ability to improve the calculation efficiency. Moreover, the engineering example demonstrates that the SLE has great influence on the natural frequency of the T-WBG, and the frequency values with the SLE have a trend of decreasing markedly in general. It is also shown that the extent of SLE effect on natural frequency varies with different boundary conditions. For the boundary condition of cantilever supported, the SLE effect on higher-order frequency is more significant than on the lower one, while for the simple supported one, the SLE effect on higher-order frequency is less marked than on the lower one.

Data Availability

The data used to support the findings of this study are available from the corresponding author upon request.

Conflicts of Interest

The authors declare that they have no conflicts of interest.

Acknowledgments

This work was supported by the Open Fund of Key Lab of Highway Construction and Maintenance Technology in Loess Region of Shanxi Transportation Research Institute (KLTLR-Y12-9). This support is appreciated.

References

- [1] G. Visnjic, D. Nozak, F. Kosel, and T. Kosel, "Shear-lag influence on maximum specific bending stiffness and strength of composite I-beam wing spar," *Proceedings of the Institution of Mechanical Engineers, Part G: Journal of Aerospace Engineering*, vol. 225, no. G5, pp. 501–511, 2011.
- [2] J. K. Suresh and V. T. Nagaraj, "Higher-order shear deformation theory for thin-walled composite beams," *Journal of Aircraft*, vol. 33, no. 5, pp. 978–986, 1996.
- [3] S. Bhalla, P. Kumar, A. Gupta, and T. K. Datta, "Simplified impedance model for adhesively bonded piezo-impedance transducers," *Journal of Aerospace Engineering*, vol. 22, no. 4, pp. 373–382, 2009.
- [4] C. Ma, S. Z. Liu, and M. Q. Wu, "Matrix analysis of composite box girder with corrugated steel webs considering shear deformation and shear lag effect," *China Journal of Highway and Transport*, vol. 31, no. 3, pp. 80–88, 2018.
- [5] C. Ma, S. Z. Liu, M. J. Wei et al., "Study on shear lag effect of single-box multi-cell PC composite box girder with corrugated steel webs," *Journal of Highway and Transportation Research and Development*, vol. 35, no. 2, pp. 62–71, 2018.
- [6] Q. g. Song and A. C. Scordelis, "Shear-lag analysis of T-, I-, and box beams," *Journal of Structural Engineering*, vol. 116, no. 5, pp. 1290–1305, 1990.
- [7] X. G. Zhong, T. Y. Zhang, X. J. Shu et al., "Shear-lag behavior of prestressed concrete box-girder bridges during balanced cantilever construction," *Advances in Concrete Construction*, vol. 5, no. 5, pp. 469–479, 2017.
- [8] S. Hu, J. Yu, C. Wei, and Z. Zhang, "Shear lag behavior and parametric sensitivity analysis of steel-concrete composite structure with double-box," *Archive of Applied Mechanics*, vol. 87, no. 9, pp. 1525–1539, 2017.
- [9] Y. Ma, Y. S. Ni, D. Xu et al., "Space grid analysis method in modelling shear lag of cable-stayed bridge with corrugated steel webs," *Steel and Composite Structures*, vol. 24, no. 5, pp. 549–559, 2017.
- [10] F. Cambrono-Barrientos, J. Díaz-del-Valle, and J.-A. Martínez-Martínez, "Beam element for thin-walled beams with torsion, distortion, and shear lag," *Engineering Structures*, vol. 143, pp. 571–588, 2017.
- [11] F. Gara, G. Ranzi, and G. Leoni, "Simplified method of analysis accounting for shear-lag effects in composite bridge decks," *Journal of Constructional Steel Research*, vol. 67, no. 10, pp. 1684–1697, 2011.
- [12] Q. g. Song and A. C. Scordelis, "Formulas for shear-lag effect of T-, I- and box beams," *Journal of Structural Engineering*, vol. 116, no. 5, pp. 1306–1318, 1990.
- [13] H. R. Evans, M. K. H. Ahmad, and V. Kristek, "Shear lag in composite box girders of complex cross-sections," *Journal of Constructional Steel Research*, vol. 24, no. 3, pp. 183–204, 1993.
- [14] H. Haji-Kazemi and M. Company, "Exact method of analysis of shear lag in framed tube structures," *Structural Design of Tall Buildings*, vol. 11, no. 5, pp. 375–388, 2003.
- [15] L. Zhu, J. Nie, and W. Ji, "Positive and negative shear lag behaviors of composite twin-girder decks with varying cross-section," *Science China Technological Sciences*, vol. 60, no. 1, pp. 116–132, 2016.
- [16] V. Kristek, H. R. Evans, and M. K. M. Ahmad, "A shear lag analysis for composite box girders," *Journal of Constructional Steel Research*, vol. 16, no. 1, pp. 1–21, 1990.
- [17] H. Cai, H. L. Lu, and Z. Tang, "Vibration properties research on curved box girder considering shear lag effects," *World Earthquake Engineering*, vol. 32, no. 4, pp. 239–244, 2016.
- [18] H. Zhang, Y. Y. Zhang, and Y. H. Zhang, "Analysis on shear deformation and shear-lag effects on twin-cell box girders," *Applied Mathematics and Mechanics*, vol. 37, no. 8, pp. 791–803, 2016.
- [19] Y. P. Zhang, H. Q. Hu, and C. X. Li, "An improvement and comparative analysis of shear lag warping displacement function in thin-walled box girder," *Chinese Journal of Applied Mechanics*, vol. 33, no. 6, pp. 1099–1105, 2016.
- [20] J. Xiao, X. Z. Li, and D. J. Liu, "Influence of different displacement functions on shear lag effect of box girders," *China Journal of Highway and Transport*, vol. 29, no. 9, pp. 90–96, 2016.
- [21] M. D. Zhou, L. Y. Li, and Y. H. Zhang, "Research on shear-lag warping displacement function of thin-walled box girders," *China Journal of Highway and Transport*, vol. 28, no. 6, pp. 67–73, 2015.
- [22] V. Kristek and J. Studnicka, "Negative shear lag in flange of plated structures," *Journal of Structural Engineering*, ASCE, vol. 117, no. 12, pp. 3553–3569, 1991.
- [23] X. L. Qin, H. B. Liu, and S. J. Wang, "Symplectic analysis of the shear lag phenomenon in a T-beam," *Journal of Engineering Mechanics*, vol. 27, no. 5, article 04014157, 2015.
- [24] Z. X. Mu and S. Y. Wei, "Analytical solution for shear lag effect of multicell thin-walled box girder," *Journal of Highway and Transportation Research and Development*, vol. 32, no. 8, pp. 93–99, 2015.
- [25] E. Reissner, "Analysis of shear lag in box beams by the principle of minimum potential energy," *Quarterly of Applied Mathematics*, vol. 4, no. 3, pp. 268–278, 1946.
- [26] J. Q. Guo, Z. Z. Fang, and X. D. Luo, "Analysis of shear lag effect in box girder bridges," *China Civil Engineering Journal*, vol. 16, no. 1, pp. 1–13, 1983.
- [27] S. T. Chang, "Prestress influence on shear-lag effect in continuous box-girder bridge," *Journal of Structural Engineering*, vol. 118, no. 11, pp. 3113–3121, 1992.
- [28] B. L. Jing, X. D. Shao, and W. G. Bao, "Research of efficient width of flange in box girder with variable cross section and long over-hanging flange," *Central South Highway Engineering*, vol. 23, no. 4, pp. 24–26, 1998.
- [29] R. T. Tenchev, "Shear lag in orthotropic beam flanges and plates with stiffeners," *International Journal of Solids and Structures*, vol. 33, no. 9, pp. 1317–1334, 1996.
- [30] Q. Z. Luo, "Calculation of the shear lag in thin walled box girder by the finite segment method," *Journal of Hunan University*, vol. 18, no. 2, pp. 33–38, 1991.
- [31] D. S. Mashat, E. Carrera, A. M. Zenkour et al., "Free vibration of FGM layered beams by various theories and finite elements," *Composites Part B-Engineering*, vol. 59, pp. 269–278, 2013.

